Transmission electron microscopy study of complex oxide scales on DIN 1.4970 steel exposed to liquid Pb-Bi eutectic

Accepted Manuscript

Title: Transmission electron microscopy study of complex oxide scales on DIN 1.4970 steel exposed to liquid Pb-Bi eutectic

Authors: E. Charalampopoulou, R. Delville, M. Verwerft, K. Lambrinou, D. Schryvers

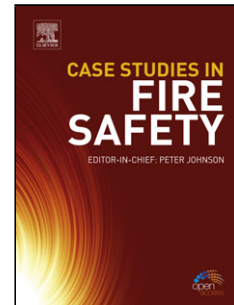Please cite this article as: Charalampopoulou E, Delville R, Verwerft M, Lambrinou K, Schryvers D, Transmission electron microscopy study of complex oxide scales on DIN 1.4970 steel exposed to liquid Pb-Bi eutectic, *Corrosion Science* (2018), https://doi.org/10.1016/j.corsci.2018.10.018

This is a PDF file of an unedited manuscript that has been accepted for publication. As a service to our customers we are providing this early version of the manuscript. The manuscript will undergo copyediting, typesetting, and review of the resulting proof before it is published in its final form. Please note that during the production process errors may be discovered which could affect the content, and all legal disclaimers that apply to the journal pertain.

# Transmission electron microscopy study of complex oxide scales on DIN 1.4970 steel exposed to liquid Pb-Bi eutectic

E. Charalampopoulou[1,2,*], R. Delville[1], M. Verwerft[1], K. Lambrinou[1], D. Schryvers[2]

[1] SCK•CEN, Boeretang 200, 2400 Mol, Belgium

[2] University of Antwerp, EMAT Research Group, Groenenborgerlaan 171, 2020 Antwerpen, Belgium

* Corresponding author. Address: Boeretang 200, 2400 Mol, Belgium. Tel.: +32 14 33 30 10
E-mail address: evangelia.charalampopoulou@sckcen.be (E. Charalampopoulou)

GRAPHICAL ABSTRACT
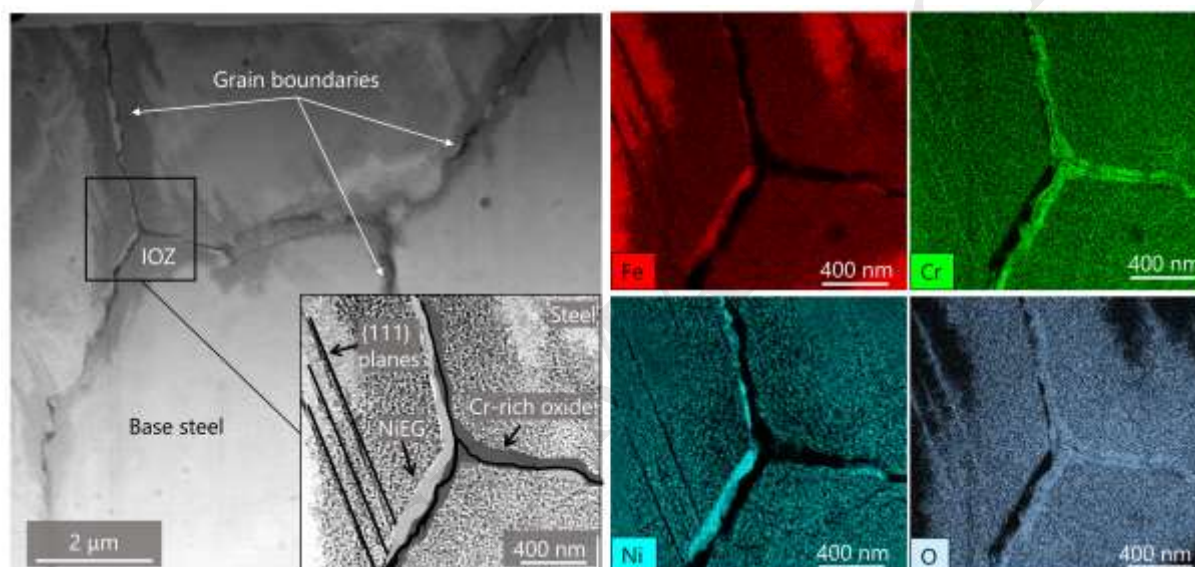
Highlights:

- At $T \leq 450°C$, Ni-rich grains (NiEGs) segregate at the steel/double oxide interface.
- At $T \geq 475°C$, an internal oxidation zone (IOZ) forms under the double oxide scale.
- The IOZ consists of two phases: a Ni-rich *fcc* phase and an FeCr-spinel phase.
- The IOZ growth relies on fast diffusion paths, such as grain and twin boundaries.

Abstract

The deployment of Gen-IV lead-cooled fast reactors requires a good compatibility between the selected structural/cladding steels and the inherently corrosive heavy liquid metal coolant. An effective liquid metal corrosion mitigation strategy involves the in-situ steel passivation in contact with the oxygen-containing Pb-alloy coolant. Transmission electron microscopy was used in this work to study the multi-layered oxide scales forming on an austenitic stainless steel fuel cladding exposed to oxygen-containing ($C_O \approx 10^{-6}$ mass%) static liquid lead-bismuth

eutectic (LBE) for 1000 h between 400 and 500 °C. The oxide scale constituents were analyzed, including the intertwined phases comprising the innermost biphasic layer.

1. Introduction

A prerequisite for the deployment of Generation-IV lead-cooled fast reactors (Gen-IV LFRs) is the good compatibility between the candidate structural/fuel cladding steels and the inherently corrosive lead-based alloy coolant [1]. The Multipurpose hYbrid Research Reactor for high-tech Applications (MYRRHA) system, currently under development at SCK•CEN, uses the lead-bismuth eutectic (LBE) alloy as both primary coolant and spallation target [2]. Despite its appealing thermal, chemical and neutronic properties [3], liquid LBE (44.5 mass% Pb +55.5 mass% Bi) leads to the degradation of nuclear grade steels due to liquid metal corrosion (LMC) effects at elevated ($T > 450$ °C) temperatures. LMC typically involves (a) elemental interdiffusion in the solid steel (i.e., outward diffusion of steel alloying elements and/or inward diffusion of oxygen dissolved in LBE), (b) chemical reactions at the steel/LBE interface (i.e., dissolution of steel alloying elements in the LBE and/or formation of oxide scales on the steel surface), and (c) transport of corrosion products away from the steel/LBE interface into the liquid LBE [4-7]. The MYRRHA LMC mitigation strategy is based on two main pillars: (a) keeping the coolant temperature below the threshold for accelerated corrosion ($T_{max} < 450$ °C), so as to suppress solution-based LBE attack, and (b) actively controlling the amount of oxygen dissolved in liquid LBE, so as to form protective oxide scales on the steel surface while excluding the formation of Pb oxides that might block flow paths in the reactor [8-10].

A number of prior studies have been dedicated to the study of the oxidation behaviour of different nuclear grade steels, both austenitic and ferritic/martensitic (F/M), as result of their exposure to oxygen-containing liquid LBE or other oxygen-containing environments (i.e., water, steam, CO_2) [11-23]. Most of the exposed steels formed a double-layered oxide scale consisting of an outer magnetite (Fe_3O_4) and an inner spinel ($Fe_xCr_{3-x}O_4$) layer. Moreover, the presence of an internal oxidation zone (IOZ) under the inner spinel scale, characterized by the presence of oxygen and the loss of steel elements, mostly iron, has been repeatedly reported for various steel grades and oxidizing media [11-14, 18-20, 24-28].

The combined use of focused ion beam (FIB) and transmission electron microscopy (TEM) in more recent studies [13, 18-20, 26, 27] revealed oxidized steel layers, the structural complexity of which had been imperceptible by scanning electron microscopy (SEM) and/or

light optical microscopy. Hosemann et al. [13], used a scanning transmission electron microscope (STEM) equipped with high angle angular dark field (HAADF) and electron dispersive X-ray spectroscopy (EDS) detectors to study the oxide scales that formed on a D9 austenitic stainless steel exposed to oxygen-containing ($C_O = 3$-5×10^{-6} mass%), flowing (2 m/s) liquid LBE for 3000 h at 550 °C, revealing an unexpectedly complex IOZ nanostructure. Similar detailed FIB/TEM studies of fine oxide structures, made of magnetite, spinel, chromia and IOZ layers, were also conducted on F/M steels exposed to LBE [18] and supercritical water [19, 20].

However, no systematic, detailed investigation of such oxide layers by means of FIB/TEM has so far been conducted as function of the steel exposure temperature. Moreover, specific open questions remain on the exact crystallographic nature and elemental composition of the nanostructures making up the IOZ in austenitic stainless steels. This knowledge is important for a profound understanding of the formation mechanism of such complex oxide layers, which is currently still lacking.

The present work investigates the oxidation behaviour of DIN 1.4970 fuel cladding steel tubes exposed for 1000 h at 400-500 °C to oxygen-containing ($C_O \approx 10^{-6}$ mass%) static liquid LBE. The complex micro/nano-structures of the oxide scales that formed on the steel surface as result of these exposures are elucidated using a combination of STEM HAADF, selected area diffraction and EDS-mapping techniques. The discussion of this work's findings is concluded by proposing a phenomenological mechanism that explains the oxidation behaviour of this steel as function of the exposure temperature.

2. Experimental

A series of experiments was designed to study the oxidation behaviour of DIN 1.4970 austenitic stainless steel fuel cladding tubes in test conditions that are relevant for the MYRRHA nominal operation ($C_O \leq 10^{-6}$ mass%, $T < 450$ °C) and higher-temperature transient conditions ($T > 450$ °C). All tests were conducted in static liquid LBE with precisely controlled oxygen concentration ($C_O \approx 10^{-6}$ mass%) and the 13 cm-long steel tube segments were isothermally exposed for 1000 h in the 400-500 °C range at select temperatures, i.e., 400, 450, 475, 500 °C (Fig. 1b). Each test used ~5 kg of as-melted LBE to ensure that LBE contamination from an earlier test did not affect the results of the next one.

The DIN 1.4970 steel cladding tubes (outer $\varnothing$ 6.55 mm, wall thickness 450 µm) tested in this work were supplied by Sandvik, Sweden, and had the following composition: 15.08±0.08% Cr, 15.04±0.15% Ni, 1.21±0.01% Mo, 1.83±0.03% Mn, 0.56±0.06% Si, and 0.49±0.02% Ti, with the balance Fe; all elemental concentrations are in mass%. The fuel cladding tubes were 24% cold worked with an unpickled, polished surface (arithmetic average roughness Ra $\leq$ 1.0 µm) [29], and were ultrasonically cleaned with acetone and ethanol prior to their insertion to the LBE bath. The test setup was a stainless steel autoclave with an inner alumina (Al_2O_3) liner to prevent the interaction of the liquid LBE with the autoclave walls (Fig. 1a). In the gas plenum, the conditioning gas was HYTEC 5 (HYTEC 5: Ar-5%H_2, Rapid Industrial Gases Ltd., UK). This gas

contained 95% Ar, 5% H_2 and minor oxygen-containing impurities (O_2 < 10 ppm, H_2O < 10 ppm) and was supplied at a constant flow rate (10 ml/min) to the autoclave from a gas bottle through a gas flow rate controller. The temperature and LBE oxygen concentration during each steel exposure were monitored by a thermocouple type K and an electrochemical oxygen sensor (air/lanthanum strontium manganese oxide (LSM) reference electrode [30]), respectively. The LBE oxygen concentration was maintained constant and at the targeted level ($C_O \approx 10^{-6}$ mass%) by means of an electrochemical oxygen pump [31]. Both electrochemical oxygen sensor and pump were developed at SCK•CEN.

Due to the fact that all steel exposures were performed in static conditions (i.e., in the absence of LBE flow), an oxygen concentration gradient was established along the bath depth direction, whereby the LBE oxygen concentration decreased from the targeted level at the tip of the oxygen pump to a significantly lower level at the gas plenum/LBE interface. In order to assess the magnitude of this gradient, a series of validation tests was conducted, whereby two oxygen sensors monitored the LBE oxygen concentration at different depths: the 1st sensor at the level of the oxygen pump, and the 2nd sensor 4 cm higher. The difference in the outputs of the two oxygen sensors was measured at different temperatures (T = 400/450/500 °C), LBE oxygen concentrations ($C_O \approx 10^{-7} - 10^{-5}$ mass%) and gases in the gas plenum (i.e., Ar-5%H_2 or Ar). It was found that despite the significant LBE oxygen concentration gradient along the bath depth during the exposures (i.e., the LBE oxygen concentration in the upper part of the bath could drop to $C_O \approx 10^{-9}$ mass%), the oxygen concentration in the LBE volume surrounding the active area of the oxygen pump was close to the targeted level (i.e., $C_O \approx 1\text{-}1.3\times10^{-6}$ mass%). This area corresponds to the bottom 4 cm of the exposed fuel cladding tubes (Fig. 1a).

At the end of each exposure, the DIN 1.4970 tubes were extracted from the autoclave and were cut in five 2 mm-long segments starting from the bottom end of the tube. This work reports only on the findings of the analysis of the bottom tube segment, as this was the tube part that was actually exposed to conditions (T, C_O) that were fairly homogeneous and close to the targeted ones in all tests. It should also be noted that the inner tube surface showed invariably signs of dissolution corrosion, which is indicative of a low oxygen concentration in the LBE volume filling the cladding tubes; the latter is attributed to the inadequate oxygen mass transport from the oxygen pump to the internal cladding tube surface under the static exposure conditions considered in this work. The bottom tube segments were cold-mounted in non-conductive resin (Struers Specifix-20), polished to a mirror surface finish (1-µm diamond paste as last step) and coated with carbon for post-test analysis by means of SEM (JSM-6610LV, JEOL) and energy-dispersive X-ray spectroscopy (EDS; XFlash detector 4010, Bruker AXS GmbH). The in-depth study of select areas of interest was conducted on thin foils made by FIB (FEI Helios Nanolab 650, FEI) by means of TEM (JEM-3010 & JEM-3000, JEOL) and STEM (FEI Tecnai Osiris S/TEM, FEI); the latter was equipped with HAADF and EDS detectors suitable for Z-contrast and elemental analysis, respectively.

3. Results

3.1. Steel exposure at 400 °C

The cladding tube segment exposed at 400 °C revealed little interaction with liquid LBE. SEM/EDS analysis showed no evidence of LBE dissolution attack and revealed the sporadic formation of magnetite 'islands' with an underlying thin FeCr-spinel layer. Moreover, these conditions did not result in the formation of an IOZ. Fig. 2 shows two STEM/ EDS elemental maps that are representative of the steel exposure at 400 °C: the first map is taken from a duplex oxide formed at the outer surface (Figs. 2a-2b) and the second from a very thin Cr oxide (Figs. 2c-2d). Figs. 2a-2b show the formation of an outer Fe-based oxide layer and an inner FeCr- spinel layer with local Ni segregations at the steel/oxide interface. On the other hand, the presence of a thin Cr-rich oxide (Figs. 2c-2d) on the largest part of the steel surface can be associated with the steel passivation and its protection against further LBE attack within the exposure timeframe of 1000 h. The average oxide scale thickness varied in the 1-3 µm range. Locally, the oxide scale thickness would reach a maximum of ~5 µm in areas with steel surface irregularities.

3.2. Steel exposure at 450 °C

By increasing the exposure temperature to 450 °C, the steel surface was covered to a large extent by a thicker (~4.5 µm) oxide scale, but once more there was no evidence of the formation of an IOZ. Steel surface areas that did not form this oxide scale were not affected by LBE dissolution attack. A FIB foil was extracted from an oxidized area of the steel surface; based on findings of previously published works [12, 23], a magnetite (Fe_3O_4) outer layer and an FeCr-spinel ($Fe_xCr_{3-x}O_4$) inner layer (occasionally with Ni-enriched metallic grains at the oxide/steel interface) would be expected to form in the oxidised parts of the steel surface. The TEM investigation of the FIB foil, combining bright field (BF) imaging with selected electron diffraction (SAED) and EDS analysis (Fig. 3), showed that the oxide scale consisted of fine-grained magnetite (Fe_3O_4) and FeCr-spinel ($Fe_xCr_{3-x}O_4$) with no clear boundary between the two phases, the one being primarily magnetite-based and the other primarily FeCr-spinel-based. The outer part of the oxide scale consisted mainly of magnetite grains interspersed with very few spinel grains (Fig. 3c). A striking feature was the presence of Ni-rich and Cr-depleted grains in the oxide scale (Fig. 3b); in principle, these grains decorated almost continuously the base steel/oxide scale interface and were also sporadically observed in the oxide scale bulk. The crystal structure of the Ni-enriched grains (NiEGs) was the *fcc* structure of the base (unaffected) steel; however, NiEGs had a different crystal orientation than their neighbouring steel grains. Table 1 provides SAED patterns, crystallographic and chemical composition information on all phases identified in the cladding tube exposed at 450 °C.

3.3. Steel exposures at 475/500 °C

As result of the exposures at 475 and 500 °C, a rather thick (maximum thickness: ~17 µm) and complex oxide scale formed on the steel surface (Fig. 4). The SEM study of the oxidised cladding tubes revealed the presence of a triple-layered oxide scale, which was more visible

after the exposure at 500 °C (Figs. 4b-4c). This oxide scale comprised a magnetite outer layer, a relatively thin intermediate FeCr-spinel layer with NiEGs, and a relatively thick internal oxidation zone (IOZ); the latter appears to have grown preferentially along specific directions in the steel bulk, presumably decorating grain boundaries (GBs) and forming "spike"-like features, such as those shown in Figs. 4b-4c. Hosemann et al. [13, 14] also reported the formation of a triple-layered oxide scale on the compositionally similar D9 steel and studied that oxide scale by means of TEM. This work investigated the structure and configuration of the oxide scales forming on DIN 1.4970 cladding tubes exposed at 475 and 500 °C by first extracting FIB foils from specific areas of interest (Figs. 4b-4c) and subsequently analysing them by TEM/STEM.

Many details of the triple-layered oxide scale were revealed by the TEM investigation of the FIB foil extracted from area 1 (Fig. 4b). Fig. 5a shows a STEM HAADF map (Z-contrast) of this area and Fig. 5c the corresponding Fe, Ni and Cr EDS elemental maps. Magnetite (Fe_3O_4) is clearly identified as the outer layer of the complex oxide scale. The presence of an LBE-filled 'pocket' and GB cracks in the magnetite layer indicate its non-protectiveness against liquid metal penetration. Underneath the magnetite layer, a ~1 μm-thick FeCr-spinel zone is visible; this zone contains Ni-enriched grains (NiEGs). Deeper into the steel, a well-established IOZ can be distinguished from the base steel, due to its oxygen enrichment and iron depletion with respect to the steel. The crystal structure of the different phases was studied by selected area electron diffraction: the SAED patterns of magnetite, FeCr-spinel grains and NiEGs were similar to those shown in Table 1. Fig. 6 shows the crystal orientation relationship between the IOZ and the base steel. The *fcc* reflections in the SAED of the base steel (Fig. 6b) are replaced by two sets of reflections in the SAED of the IOZ (Fig. 6c). The change in composition from the base steel to the IOZ is shown in the EDS line scan across the boundary between the two phases (Fig. 6d). This EDS line scan shows that the IOZ is characterised by an overall loss of Fe as well as by the alteration of areas enriched in Cr and O with areas enriched in Ni.

Selected area diffraction (Fig. 7b) showed the establishment of the IOZ at the tip of the "spike"-like feature that was also selected for FIB foil extraction (area 2, Fig. 4c). Fig. 8 shows the Z-sensitive STEM HAADF image of the IOZ at this location, alongside the corresponding EDS elemental maps that revealed an intricate network of alternating Ni-Fe-Cr and Cr-Fe-O zones. A similar inner oxide layer structure was previously reported by Hosemann et al. [13], as result of the oxidation of a D9 stainless steel fuel cladding tube exposed for 3000 h at 550 °C to flowing liquid LBE with $C_O \approx$ 3-5×10^{-6} mass%. These authors tentatively attributed the formation of the intricate oxide layer structure to a spinodal decomposition, but were unable to resolve its crystal structure by means of electron diffraction.

The careful analysis of two SAED patterns of the IOZ (position b, Fig. 7a), taken along two tilt orientations, showed that most reflections could be attributed to two distinctly different phases: a Ni-enriched phase with a simple *fcc* lattice (*Fm-3m*, *a*=0.35 nm, red dots in schemas of Fig. 9), and a Cr-enriched phase with an *fcc* spinel lattice (*Fd-3m*, *a*=0.83 nm, blue dots in schemas of Fig. 9). The reflections from these two phases appear as the more intense spots in

the SAED patterns of Fig. 9. All other reflections could be attributed to multiple diffraction from the two phases, which is a likely event, since the electron beam is expected to encounter both phases multiple times in its path across the FIB foil thickness; moreover, the high-resolution STEM HAADF study of the IOZ suggested that its two constituent phases are intertwined on the nanoscale, an observation that indirectly supports the hypothesis by Hosemann et al. [13] that the IOZ might have resulted from a spinodal decomposition.

Another salient feature of the IOZ growth into steel GBs is the formation of "needle"-like features that nucleate in the IOZ and develop away from it and into the base steel, following two specific crystallographic planes, i.e., the $\{\bar{1}11\}$ and the $\{1\bar{1}1\}$ (Fig. 7a). These planes become visible by leaving dark, line-like traces in the IOZ, the orientation of which corresponds to <111> closed-packed planes, as confirmed by looking along the <011> zone axis (Z.A.). A closer view of one "needle" is provided in Fig. 10, which combines an STEM HAADF image with EDS elemental maps and a line scan of the feature of interest. The EDS elemental maps (Fig. 10b) show that the "needle" is characterized by an overall enrichment in O and depletion in Fe, while the Cr and Ni concentrations are subjected to local fluctuations, whereupon areas richer in Cr are poorer in Ni and vice versa. The latter is confirmed by the EDS line scan (Fig. 10c), which reveals a match between areas enriched in both Cr and O and areas depleted in Ni. Moreover, the EDS elemental maps show that Ni has segregated around Fe-depleted areas (Fig. 10b).

The role played by GBs in elemental diffusion is clearly illustrated in Fig. 11. The Z-contrast STEM HAADF picture (Fig. 11a) and the detailed EDS elemental maps at a triple point (Fig. 11c) reveal GBs enriched in O, depleted in Fe, and decorated by the same IOZ structure that was described earlier. Furthermore, several GB segments are characterized by the combined local segregation of Ni with Fe next to the combined local segregation of Cr with O (Fig. 11c). In these areas, the Ni and Cr concentrations are higher than the respective concentrations in the non-affected parts of the steel grains (still visible in the upper left and right corners of Fig. 11c).

The findings of this work are summarized in the idealized drawings of Fig. 12, which attempts to propose a phenomenological oxidation mechanism for the DIN 1.4970 fuel cladding steel exposed for 1000 h at 400-500 °C to static liquid LBE with $C_O \approx 10^{-6}$ mass%. The proposed mechanism identifies two different temperature regimes: one for $T \leq 475$ °C (Figs. 12I.a-12I.c) and one for $T \geq 475$ °C (Figs. 12II.a-12II.c). The main difference between the two regimes is the IOZ formation, which was observed only as result of the high-temperature exposures (i.e., $T \geq 475$ °C). The findings of this work are discussed in detail in the next section and are concluded by proposing an oxidation mechanism for the DIN 1.4970 cladding steel.

4. Discussion

The onset of the oxidation process involves chemical reactions between the oxygen that is dissolved in liquid LBE and the Fe and Cr in the steel; the reactions occur at the steel surface,

at rates controlled by the temperature-dependent outward diffusion of Fe in the solid phase (e.g., magnetite [17]) (Figs. 12I.b and 12II.b). As shown in this work, high exposure temperatures ($T \geq 475$ °C) lead to thick, large-grained magnetite scales, the growth of which is accompanied by thick Fe-depleted zones, corresponding to the IOZ, in the underlying steel bulk (Fig. 12II.c). Underneath the magnetite scales, there is sufficient O and free space, due to the departed Fe, to form micrometre-sized FeCr-spinel grains. The thickness of the FeCr-spinel scale remains relatively small (1-2 μm), irrespective of the test temperature (Figs. 4-6, 12). The network of vacancies caused by the outward diffusion of Fe facilitates the inward diffusion of O, resulting in the formation of the IOZ (Figs. 5-8, 10, 11, 12II.b-12II.c) [18, 32]. Along its diffusion path into the steel, O encounters the remaining Cr, Fe and Ni, oxidizing the former two but not reacting with Ni, for which it has lower affinity (i.e., NiO is thermodynamically stable at higher oxygen potentials than all Fe/Cr-based oxides [33]). Elemental diffusion is slower in the low temperature regime ($T \leq 450$ °C); therefore, the inward O diffusion and outward Fe diffusion are confined within the FeCr-spinel layer, which is paired with a small-grained magnetite layer of comparable thickness (Figs. 2-3, 12I.b-12I.c). Contrary to the samples exposed at higher temperatures ($T \geq 475$°C), no clear boundary exists between magnetite and FeCr-spinel phases for the sample exposed at 450°C. These findings suggest the existence of a threshold temperature between 450 and 475 °C, above which both IOZ formation and magnetite growth are promoted. Closer to the outer oxide surface, the presence of individual magnetite grains is predominant. However, Fe oxide grains with or without Cr are found throughout the oxide scale, making the clear distinction between the standard oxide layers (magnetite/FeCr-spinel) impossible.

At all temperatures, Ni does not oxidize and remains as *fcc* Ni-enriched grains (NiEGs) in the FeCr-spinel layer (Figs. 3, 5-8, 11, 12I.c, 12II.c). NiEGs have been reported by several authors [11-13, 21, 23, 34] and, in this work, they are attributed to a segregation process caused by the fact that Fe and Cr diffuse outwards faster than Ni [35]. The outward diffusing Fe and Cr react with the inward diffusing O to form the outer magnetite and inner FeCr-spinel layers, while the sluggishly outward diffusing Ni segregates at the steel/oxide interface in its metallic form, since the formation of NiO grains would have required an appreciably higher supply of oxygen [33]. Taking the above into account, the frequently observed segregation of Ni-rich precipitates at the steel/spinel interface is caused by the Ni redistribution occurring during steel oxidation; the latter is affected by the relative diffusivity of the steel alloying elements in the steel as well as their relative affinity to the inward diffusing oxygen and its local concentration in the steel. The outward flux of Fe and Cr atoms creates vacancies in the steel, facilitating the inward flux of O atoms. The presence of O in the steel bulk leads to local steel oxidation, an aspect of which is the formation of the IOZ structure. At 450 °C, the largest NiEGs decorate the base steel/spinel interface (Figs. 3b, 12I.c), presumably forming a diffusion barrier layer that decelerates the overall oxidation process; this hypothesis is corroborated by the absence of an IOZ beyond the continuous NiEG 'barrier'. The lack of a continuous NiEG 'barrier' in the steel tubes oxidised at $T \geq 475$ °C might in part explain the establishment of an IOZ beyond the depth of highest NiEG density (Figs. 5, 6, 12II.c).

The IOZ is typically characterized by Fe depletion and O enrichment with respect to the base steel and has been observed in austenitic stainless steels and F/M steels exposed to liquid LBE or other oxygen-containing environments (i.e., water, steam) at elevated temperatures ($T \geq 500$ °C) and high oxygen concentrations ($C_O \geq 10^{-6}$ mass%) [11-14, 19, 20, 24-27, 36]. Despite its frequent observation, a limited number of studies on its fine structure can be found for F/M steels [18-20, 26, 27] and only one study for austenitic stainless steels [13, 28]. The nanoscale biphasic nature of the IOZ in austenitic stainless steels has been previously only reported by Hosemann et al. [13] for a D9 stainless steel fuel cladding exposed at 550 °C to flowing LBE with $C_O = 3-5 \times 10^{-6}$ mass%. However, these authors were not successful in identifying the crystal structure of the phases present in the IOZ due to the complex SAED pattern created by multiple diffraction through the biphasic nanostructure. The present work shows that the IOZ found in DIN 1.4970 steel tubes exposed at 475 and 500 °C to static LBE with $C_O \approx 10^{-6}$ mass% comprises two phases, i.e., an Cr-Fe-O spinel oxide phase (*fcc* structure) and a Ni-enriched Fe-Ni-Cr metallic phase (*fcc* structure). These two phases are identical with the phases FeCr-spinel and NiEG that were found in a coarser format in the inner FeCr-spinel layer (Figs. 5a, 6a, 12II.c). Elemental analysis clearly shows the absence of Ni in the Cr-Fe-O spinel phase, while the O signal is more strongly correlated with the Cr-rich phase (Figs. 10b-10c). The significant O background signal that remains in EDS elemental maps (e.g., O map in Fig. 8c) can be attributed to the bremsstrahlung signal at the low O $K\alpha$ energy and its overlap with the Cr $L\alpha$ peak, the latter element being present in both phases. Based on the above, there is no real experimental evidence of the presence of O in the Ni-rich Fe-Ni-Cr metallic *fcc* phase; taking also into account the low affinity of Ni to O, it is assumed that O is not present in this phase. Assuming that the phases in the IOZ observed in this work are similar to those in the closely-related D9 steel grade, the findings of this work have been explained from an alternative standpoint than the one by Hosemann et al. [13] that the Ni-enriched phase, whose crystallography was not resolved in the work of these authors, contains O.

The crystal structure (*fcc*) and orientation of the Ni-rich phase is the same as the steel grain in which the IOZ has propagated (Figs. 6, 7, 9). The Cr-rich spinel structure also keeps the same cube-on-cube orientation relationship. This suggests that O diffuses into the sub-stoichiometric (due to Fe and Cr vacancies) *fcc* steel lattice, where it triggers the heterogeneous nucleation of the Cr-rich FeCr-spinel by preferentially oxidizing Fe and Cr. The selective removal of Fe and Cr from the steel grain leads to the formation of the Ni-rich metallic phase, which maintains the crystal orientation of the 'parent' grain. The idea that the crystal orientation of the 'parent' steel is maintained in the IOZ was first encountered in the work of Hosemann et al. [13, 28]. Also worthwhile mentioning is the lack of elemental gradients along the IOZ depth (Fig. 6d), which suggests that when the right elemental ratio (Fe/Cr/O) is reached in the steel, it spontaneously decomposes into the Cr-rich spinel and the Ni-rich metallic phases comprising the IOZ. At the moment, there are no thermodynamic calculations predicting a spinodal decomposition – as proposed by Hosemann et al. [13] – in the Fe-Cr-Ni-O system, so the exact nature of the IOZ formation mechanism remains a matter of speculation.

Similar to the phases observed in the inner FeCr-spinel layer, the higher affinity of Fe and Cr to O as compared to Ni explains the observed phase separation in the IOZ. The scale of phase separation differs between the IOZ and the inner FeCr-spinel layer: nanometre scale in the IOZ and micrometre scale in the spinel layer. One might attribute the difference in the scale of phase separation to the coarsening of the biphasic structure in the spinel layer with time, as opposed to the IOZ that formed later and thus remains ultrafine; such coarsening phenomena are driven by the continuous supply of O and the tendency of the system to minimise its Gibbs free energy by decreasing the surface energy associated with the formation of a nano-sized IOZ biphasic structure. It is, therefore, reasonable to expect that prolonged steel exposures or exposures to higher temperatures would coarsen the IOZ. Similarly, increasing the LBE oxygen concentration is likely to increase the IOZ thickness for comparable test conditions (T, time) or even oxidize the Ni-rich constituent of the IOZ, thereby decomposing this biphasic structure into two different oxide phases separated by distinct grain boundaries.

This work also provided evidence of the role played by grain and twin boundaries in the oxidation behaviour of the DIN 1.4970 fuel cladding steel; these boundaries act as accelerated paths for elemental diffusion (Fe, O) in the IOZ. Ni-rich *fcc* grains and Cr-rich spinel oxides were found to decorate GBs in the IOZ (Figs. 8, 11). The formation of these two phases decorating the GBs is reminiscent of the two phases observed on a much finer scale in the neighbouring IOZ. It is noteworthy that, in the zones of elemental segregation at GBs, Fe was not detected in the Cr oxide phase and Cr was not detected in the Ni-Fe metallic phase. Such observation would not be possible in the IOZ due to its nanocrystallinity, which would result in an overlap of the EDS elemental maps of the two phases. The relatively high segregation of Ni and Cr at the GBs suggests some degree of diffusion of Ni and Cr from the grain bulk towards the GB. Once again, only Cr readily oxidizes whereas Ni remains together with Fe in metallic form.

Some of the features of the oxide growth and evolution discussed above are schematically summarized in Fig. 12. Two temperature regimes are depicted: one that grows only magnetite and FeCr-spinel layers (low temperature) (Figs. 12I.a-12I.c) and one that also favours the creation of an IOZ (high temperature) (Figs. 12II.a-12II.c). Differences in the relative thickness of the oxide scale layers are highlighted throughout the schematics. It shows that the presence of the IOZ is associated with the presence of a thick magnetite scale (Fig. 12II.c). The FeCr-spinel layer grows from the steel surface inwards, while the IOZ structure originates from local interactions between the permeating oxygen and its surrounding Fe/Cr/Ni matrix.

5. Conclusions

DIN 1.4970 austenitic stainless steel fuel cladding tubes were exposed to static liquid LBE with $C_O \approx 10^{-6}$ mass% for 1000 h at 400, 450, 475 and 500 °C. The complex oxide scales that formed as result of these exposures were investigated by SEM, FIB/TEM and STEM HAADF. The following findings of this work were used to propose a steel oxidation mechanism:

1. At $T \leq 475$ °C, a double-layered oxide scale was observed along with the segregation of *fcc* Ni-enriched grains (NiEGs) at the oxide/steel interface. The oxide scale consisted of a magnetite (Fe_3O_4) outer layer and an Fe-Cr-O spinel inner layer.

2. At $T \geq 475$ °C, the double oxide scale, comprising a thick magnetite layer and a much thinner FeCr-spinel layer, was underlain by a thick internal oxidation zone (IOZ) depleted in Fe and enriched in O.

3. STEM HAADF, EDS and SAED revealed the crystal structure and composition of the two constituent IOZ phases, which were interwoven at the nanoscale. One phase was enriched in Ni and was structurally similar to the NiEGs (*fcc*), while the other was a Cr-enriched FeCr-spinel (*fcc*). Both phases shared the same crystallographic orientation with the underlying steel matrix.

4. EDS elemental mapping suggested that the growth of the IOZ relied on the accelerated elemental diffusion, in particular of O and Fe, and ensuing segregation of Ni and Cr along grain and twin boundaries in the base steel.

Further unravelling of the DIN 1.4970 steel oxidation behaviour requires additional short-term exposures, so as to conclude whether the formation of the IOZ follows the formation of the top oxide scale or they both nucleate simultaneously.

Acknowledgments

Data Availability

The raw/processed data required to reproduce these findings cannot be shared at this time, as the data form part of another ongoing study.

References

[1] C.F. Smith, L. Cinotti, Lead-cooled fast reactor A2, in: Handbook of Generation IV Nuclear Reactors, Woodhead Publishing, 2016, pp. 119-155.

[2] H. Aït Abderrahim, P. Baeten, D. De Bruyn, R. Fernandez, MYRRHA – A multi-purpose fast spectrum research reactor, Energy Conversion and Management, 63 (2012) 4-10.

[3] Handbook on Lead-Bismuth Eutectic Alloy and Lead Properties, Materials compatibility, Thermal-hydraulics and Technologies, OECD, NEA 2007.

[4] J. Weeks, H.S. Isaacs, Corrosion and deposition of steels and nickel-base alloys in liquid sodium, in: M.G. Fontana, R.W. Staehle (Eds.) Advances in Corrosion Science and Technology, Plenum Press, 1973.

[5] N. Li, Lead-alloy coolant technology and materials – technology readiness level evaluation, Progress in Nuclear Energy, 50 (2008) 140-151.

[6] J. Zhang, P. Hosemann, S. Maloy, Models of liquid metal corrosion, Journal of Nuclear Materials, 404 (2010) 82-96.

[7] K. Lambrinou, E. Charalampopoulou, T. Van der Donck, R. Delville, D. Schryvers, Dissolution corrosion of 316L austenitic stainless steels in contact with static liquid lead-bismuth eutectic (LBE) at 500 °C, Journal of Nuclear Materials, 490 (2017) 9-27.

[8] J. Zhang, A review of steel corrosion by liquid lead and lead–bismuth, Corrosion Science, 51 (2009) 1207-1227.

[9] A. Weisenburger, C. Schroer, A. Jianu, A. Heinzel, J. Konys, H. Steiner, G. Müller, C. Fazio, A. Gessi, S. Babayan, A. Kobzova, L. Martinelli, K. Ginestar, F. Balbaud-Célerier, F.J. Martín-Muñoz, L. Soler Crespo, Long term corrosion on T91 and AISI1 316L steel in flowing lead alloy and corrosion protection barrier development: Experiments and models, Journal of Nuclear Materials, 415 (2011) 260-269.

[10] C. Schroer, O. Wedemeyer, J. Konys, Aspects of minimizing steel corrosion in liquid lead-alloys by addition of oxygen, Nuclear Engineering and Design, 241 (2011) 4913-4923.

[11] X. Chen, J.F. Stubbins, P. Hosemann, A.M. Bolind, Analysis of corrosion scale structure of pre-oxidized stainless steel 316 in molten lead bismuth eutectic and the relation to impedance spectroscopy response, Journal of Nuclear Materials, 398 (2010) 172-179.

[12] A. Heinzel, A. Weisenburger, G. Müller, Corrosion behavior of austenitic steels in liquid lead bismuth containing $10-6$wt% and $10-8$wt% oxygen at 400–500°C, Journal of Nuclear Materials, 448 (2014) 163-171.

[13] P. Hosemann, R. Dickerson, P. Dickerson, N. Li, S.A. Maloy, Transmission electron microscopy (TEM) on oxide layers formed on D9 stainless steel in lead bismuth eutectic (LBE), Corrosion Science, 66 (2013) 196-202.

[14] P. Hosemann, M. Hawley, D. Koury, J.G. Swadener, J. Welch, A.L. Johnson, G. Mori, N. Li, Characterization of oxide layers grown on D9 austenitic stainless steel in lead bismuth eutectic, Journal of Nuclear Materials, 375 (2008) 323-330.

[15] D. Koury, A.L. Johnson, T. Ho, J.W. Farley, Analysis of bi-layer oxide on austenitic stainless steel, 316L, exposed to Lead–Bismuth Eutectic (LBE) by X-ray Photoelectron Spectroscopy (XPS), Journal of Nuclear Materials, 440 (2013) 28-33.

[16] H. Steiner, C. Schroer, Z. Voß, O. Wedemeyer, J. Konys, Modeling of oxidation of structural materials in LBE systems, Journal of Nuclear Materials, 374 (2008) 211-219.

[17] J. Zhang, N. Li, Oxidation mechanism of steels in liquid-lead alloys, Oxidation of Metals, 63 (2005) 353-381.

[18] Z. Ye, P. Wang, H. Dong, D. Li, Y. Zhang, Y. Li, Oxidation mechanism of T91 steel in liquid lead-bismuth eutectic: with consideration of internal oxidation, Scientific Reports, 6 (2016) 35268.

[19] J. Bischoff, A.T. Motta, Oxidation behavior of ferritic–martensitic and ODS steels in supercritical water, Journal of Nuclear Materials, 424 (2012) 261-276.

[20] J. Bischoff, A.T. Motta, EFTEM and EELS analysis of the oxide layer formed on HCM12A exposed to SCW, Journal of Nuclear Materials, 430 (2012) 171-180.

[21] C. Schroer, O. Wedemeyer, J. Novotny, A. Skrypnik, J. Konys, Long-term service of austenitic steel 1.4571 as a container material for flowing lead–bismuth eutectic, Journal of Nuclear Materials, 418 (2011) 8-15.

[22] L. Martinelli, C. Desgranges, F. Rouillard, K. Ginestar, M. Tabarant, K. Rousseau, Comparative oxidation behaviour of Fe-9Cr steel in CO_2 and H_2O at 550°C: Detailed analysis of the inner oxide layer, Corrosion Science, 100 (2015) 253-266.

[23] O. Yeliseyeva, V. Tsisar, G. Benamati, Influence of temperature on the interaction mode of T91 and AISI 316L steels with Pb–Bi melt saturated by oxygen, Corrosion Science, 50 (2008) 1672-1683.

[24] C. Schroer, J. Konys, T. Furukawa, K. Aoto, Oxidation behaviour of P122 and a 9Cr–2W ODS steel at 550°C in oxygen-containing flowing lead–bismuth eutectic, Journal of Nuclear Materials, 398 (2010) 109-115.

[25] H. Glasbrenner, J. Konys, G. Mueller, A. Rusanov, Corrosion investigations of steels in flowing lead at 400°C and 550°C, Journal of Nuclear Materials, 296 (2001) 237-242.

[26] H. Dong, P. Wang, D. Li, Y. Li, Effect of pre-deformation on the oxidation resistance of a high Si ferritic/martensitic steel in oxygen-saturated stagnant lead-bismuth eutectic at 550°C, Corrosion Science, 118 (2017) 129-142.

[27] J. Wang, S. Lu, L. Rong, D. Li, Y. Li, Effect of silicon on the oxidation resistance of 9wt.% Cr heat resistance steels in 550°C lead-bismuth eutectic, Corrosion Science, 111 (2016) 13-25.

[28] P. Hosemann, M. Hawley, G. Mori, N. Li, S.A. Maloy, AFM and MFM characterization of oxide layers grown on stainless steels in lead bismuth eutectic, Journal of Nuclear Materials, 376 (2008) 289-292.

[29] R. Delville, E. Stergar, M. Verwerft, Results of a new production of nuclear-grade 1.4970 15-15Ti stainless steel fuel cladding tubes for GEN IV reactors, in: 22nd International Conference on Nuclear Engineering (ICONE22), ASME, Prague, Czech Republic, 2014.

[30] J. Lim, G. Manfredi, A. Mariën, J. Van den Bosch, Performance of potentiometric oxygen sensors with LSM-GDC composite electrode in liquid LBE at low temperatures, Sensors and Actuators B: Chemical, 188 (2013) 1048-1054.

[31] J. Lim, G. Manfredi, S. Gavrilov, K. Rosseel, A. Aerts, J. Van den Bosch, Control of dissolved oxygen in liquid LBE by electrochemical oxygen pumping, Sensors and Actuators B: Chemical, 204 (2014) 388-392.

[32] L. Martinelli, F. Balbaud-Célérier, A. Terlain, S. Bosonnet, G. Picard, G. Santarini, Oxidation mechanism of an Fe–9Cr–1Mo steel by liquid Pb–Bi eutectic alloy at 470 °C (Part II), Corrosion Science, 50 (2008) 2537-2548.

[33] C. Schroer, J. Konys, Physical Chemistry of Corrosion and Oxygen Control in Liquid Lead and Lead-Bismuth Eutectic, in: Wissenschaftliche Berichte FZKA 7364, Forschungszentrum Karlsruhe, 2007.

[34] J. Zhang, N. Li, Y. Chen, A.E. Rusanov, Corrosion behaviors of US steels in flowing lead–bismuth eutectic (LBE), Journal of Nuclear Materials, 336 (2005) 1-10.

[35] S.J. Rothman, L.J. Nowicki, G.E. Murch, Self-diffusion in austenitic Fe-Cr-Ni alloys, Journal of Physics F: Metal Physics, 10 (1980) 383.

[36] K. Lambrinou, V. Koch, G. Coen, J. Van den Bosch, C. Schroer, Corrosion scales on various steels after exposure to liquid lead–bismuth eutectic, Journal of Nuclear Materials, 450 (2014) 244-255.
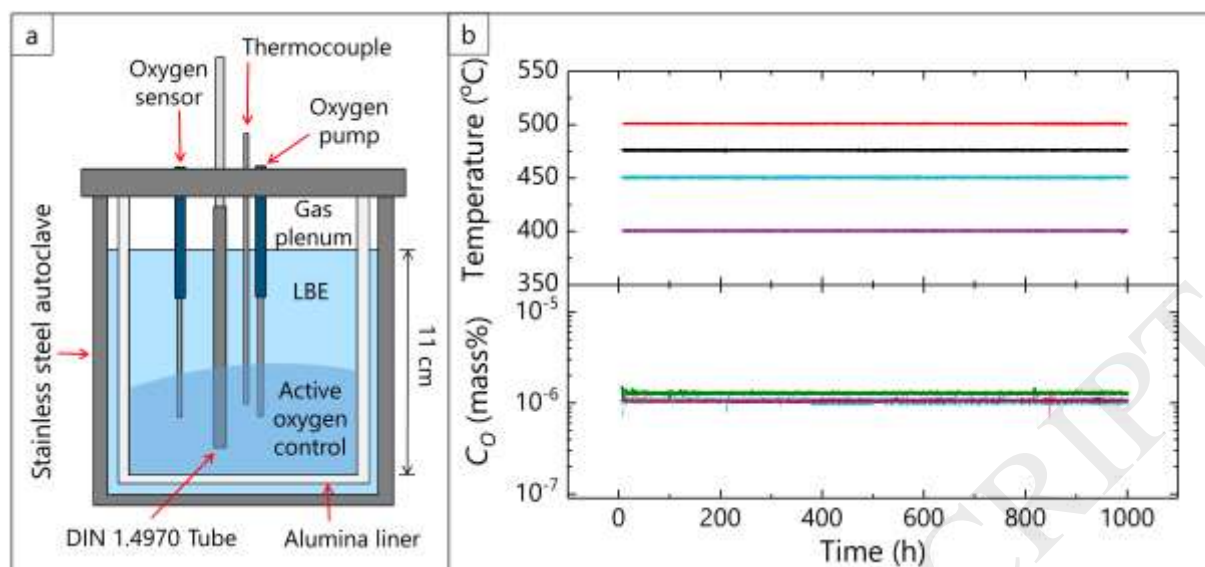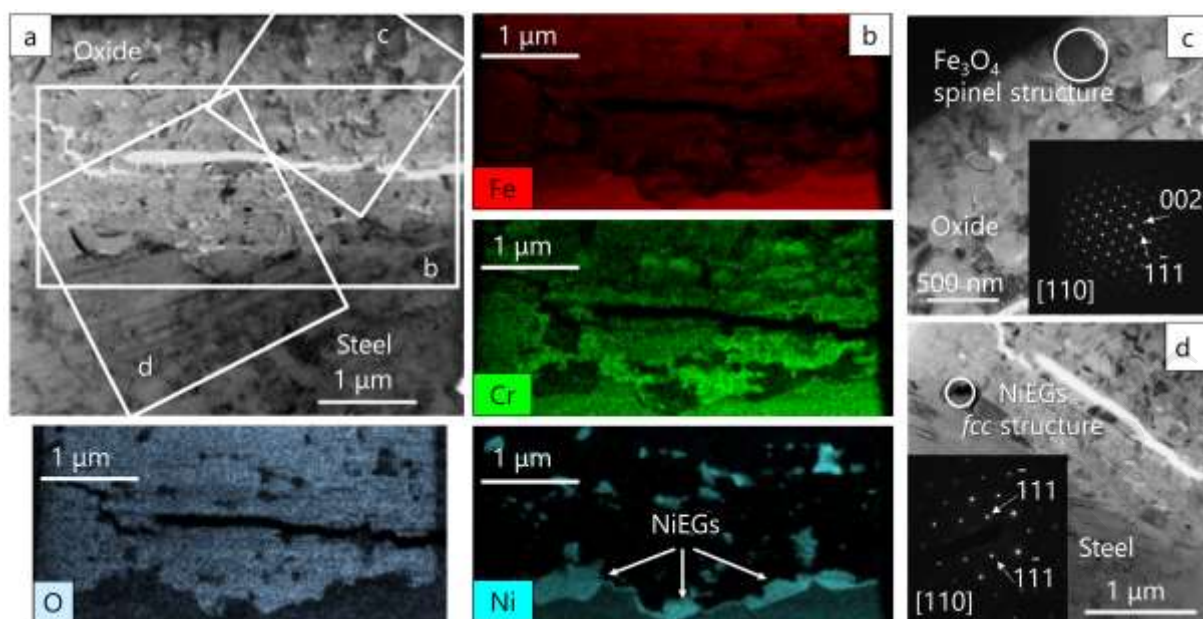
Fig. 1. (a) Schematic representation of the experimental setup used in this work. (b) Overview of the conditions during the exposures performed in this work.
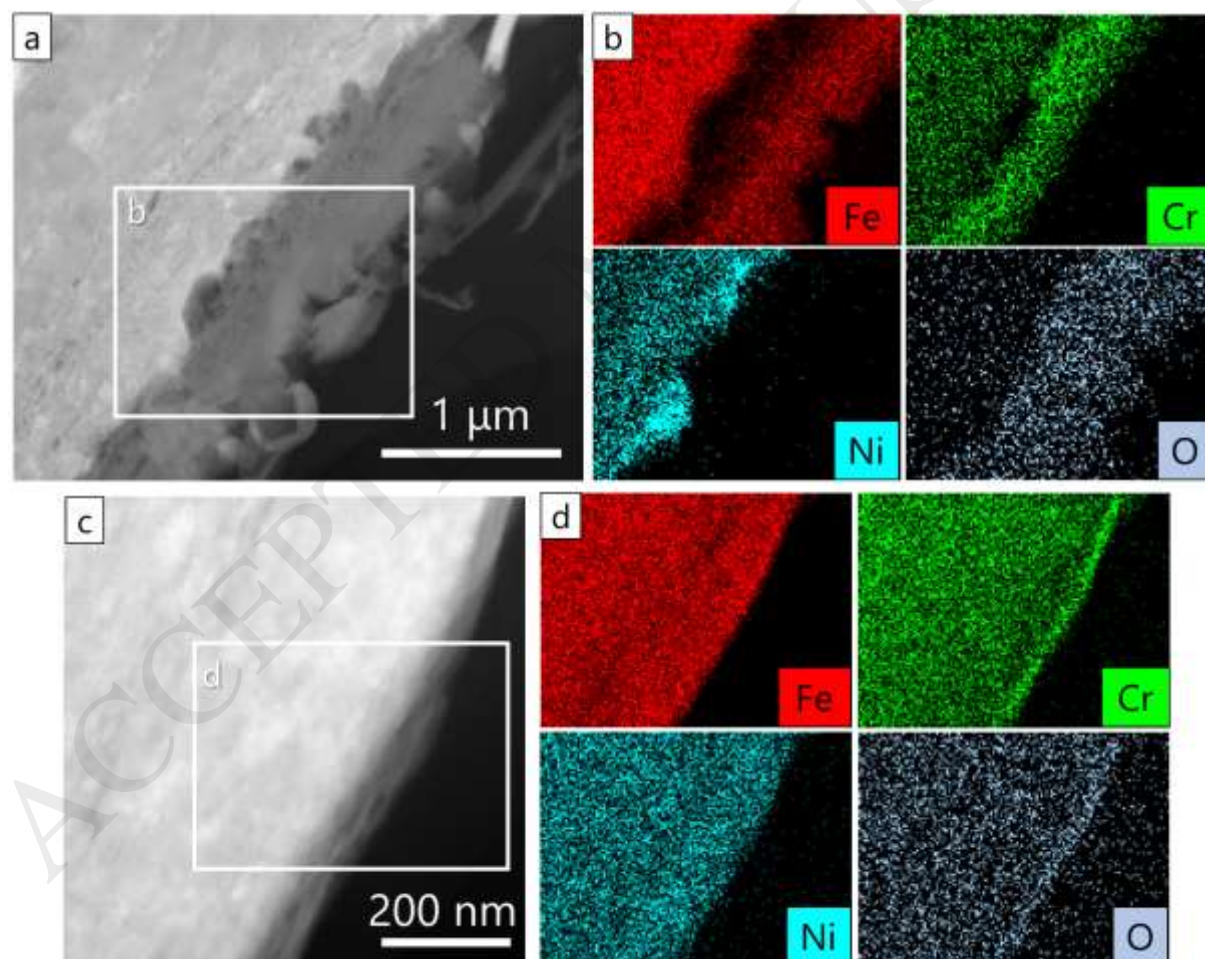

Fig. 2. (a) TEM BF image and (b) STEM/EDS elemental maps of the FIB foil extracted from a representative oxide at 400 °C. (c) TEM BF and (b) STEM/EDS elemental maps of a thin oxide formed at the surface of the DIN 1.4970 tube.

Fig. 3. (a) TEM BF image and (b) STEM/EDS elemental maps of the FIB foil extracted from an oxidised area on the DIN 1.4970 tube exposed at 450 °C. (c) TEM BF and SAED pattern of a magnetite (Fe_3O_4) grain (spinel *fcc* structure). (d) TEM BF and SAED pattern of a Ni-enriched grain (NiEG; *fcc* structure) at the steel/oxide interface.
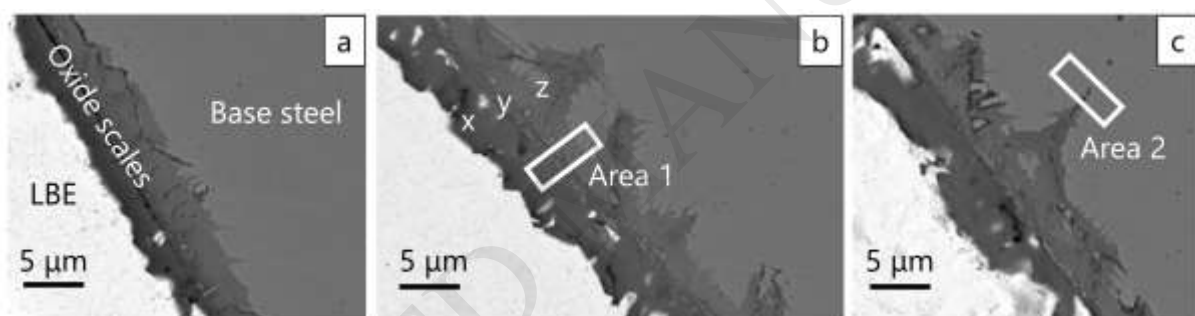
Fig. 4. BSE images of the oxide scale formed on DIN 1.4970 tubes exposed at 475 °C (a) and 500 °C (b,c). In both cases, the oxide scale comprises an outer oxide layer (x), an intermediate oxide layer (y), and an IOZ (z). Rectangles indicate the selected areas of interest for FIB foil extraction.

16
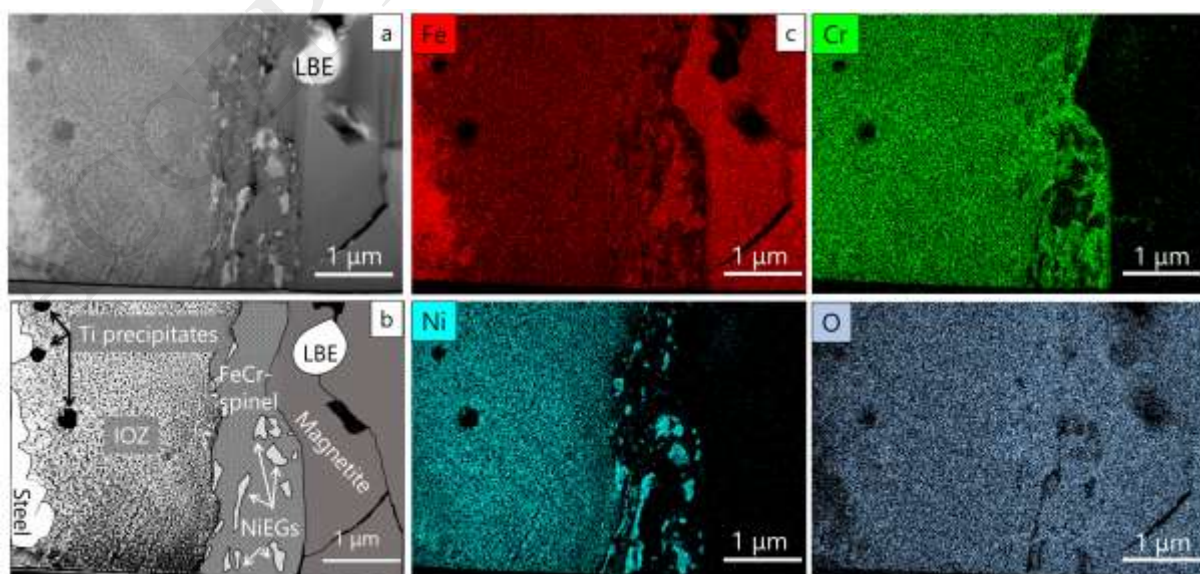
Fig. 5. (a) STEM HAADF image, (b) idealised drawing, and (c) STEM/EDS elemental maps of the complex oxide scale (area 1) on the DIN 1.4970 tube exposed at 500 °C.
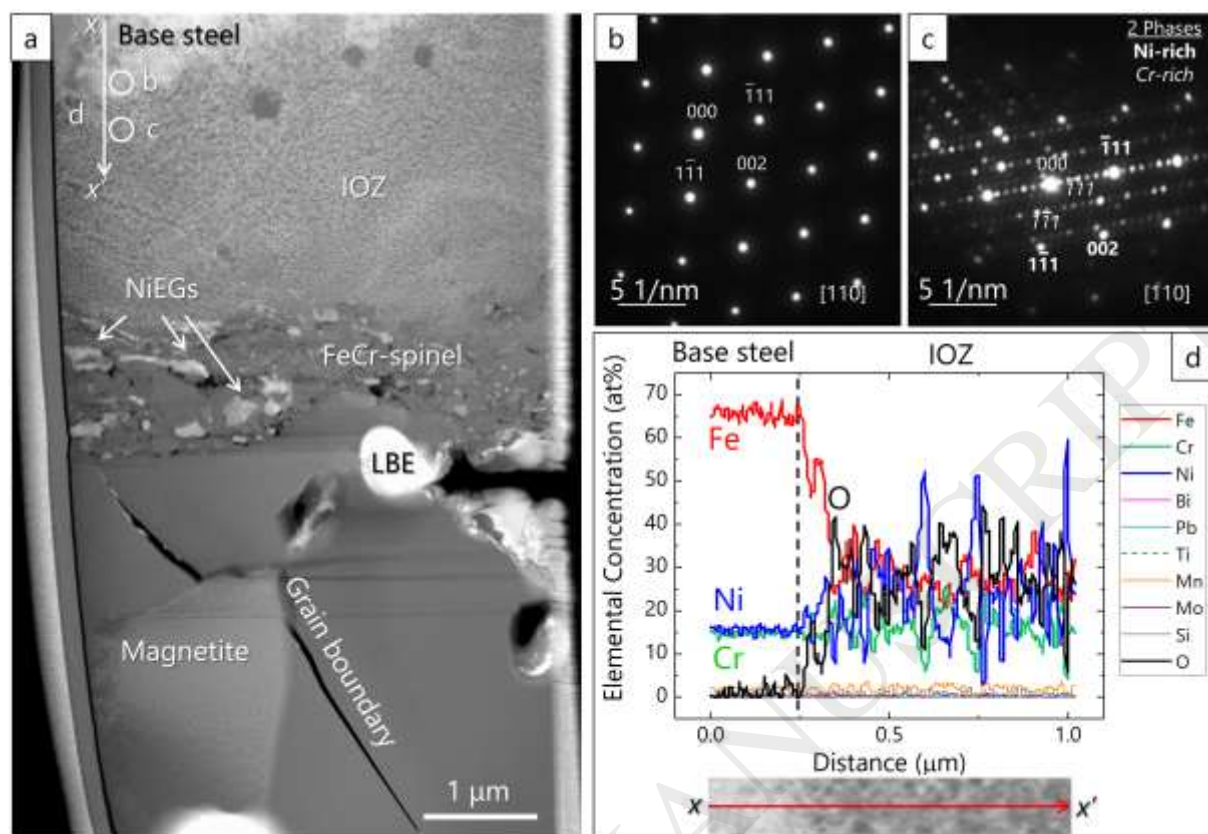
Fig. 6. (a) STEM HAADF overview of the FIB foil from area 1 in the DIN 1.4970 tube exposed at 500 °C, (b) SAED pattern of the base steel, (c) SAED pattern of the IOZ, and (d) STEM/EDS line scan across both the base steel and the IOZ.
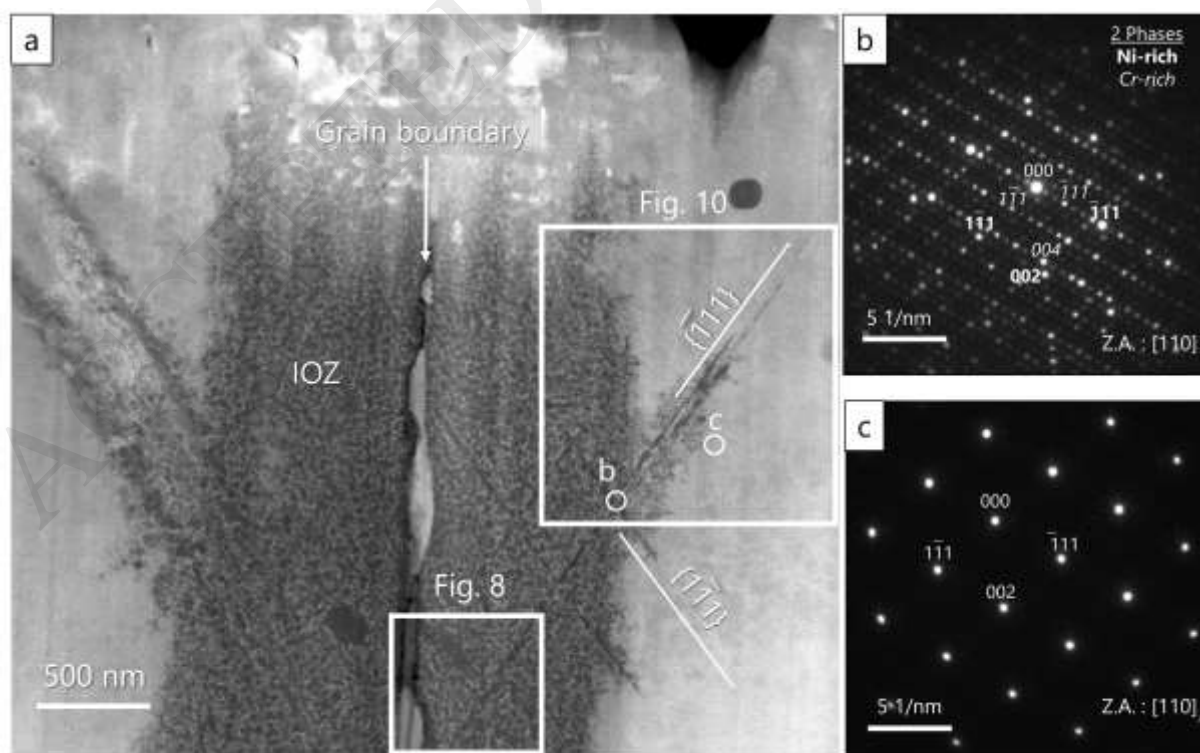
Fig. 7. (a) STEM HAADF overview of the FIB foil from area 2 in the DIN 1.4970 tube exposed at 500 °C, showing the IOZ growth along a steel grain boundary, (b) SAED pattern of the IOZ, and (c) SAED pattern of the base steel.
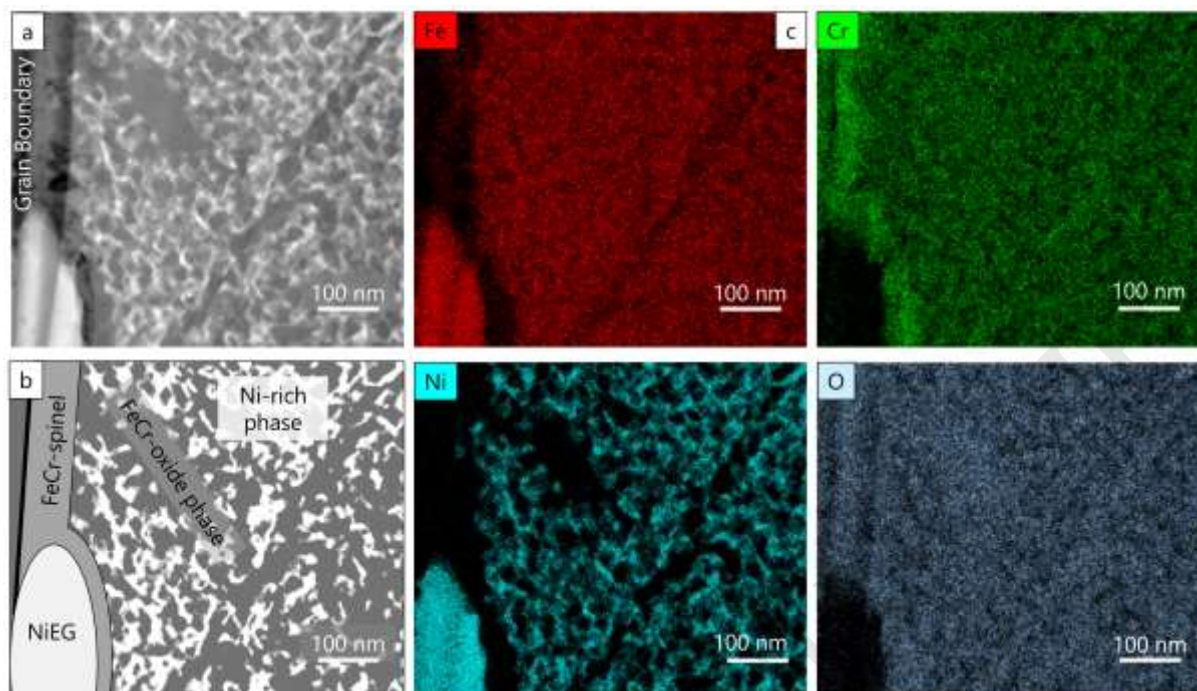
Fig. 8. (a) High-resolution STEM HAADF overview, (b) idealised drawing, and (c) EDS elemental maps showing the growth of the IOZ along a steel grain boundary.
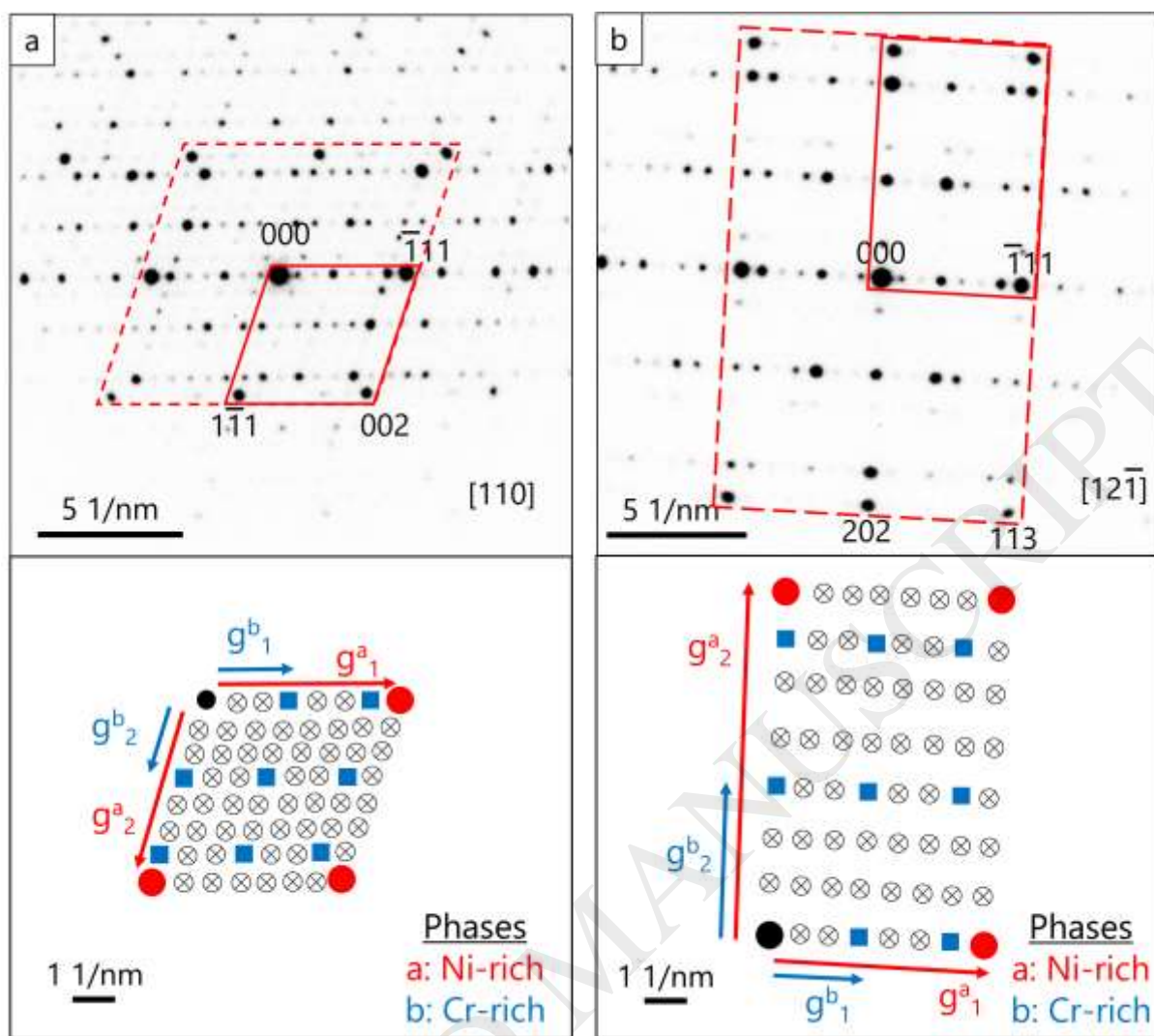
Fig. 9. SAED patterns of the IOZ and corresponding schematics for (a) the [**110**] zone axis (Z.A.) (same Z.A. as in Fig. 7b) and (b) the [**12$\bar{1}$**] Z.A., as a part of a tilting experiment in selected area diffraction.
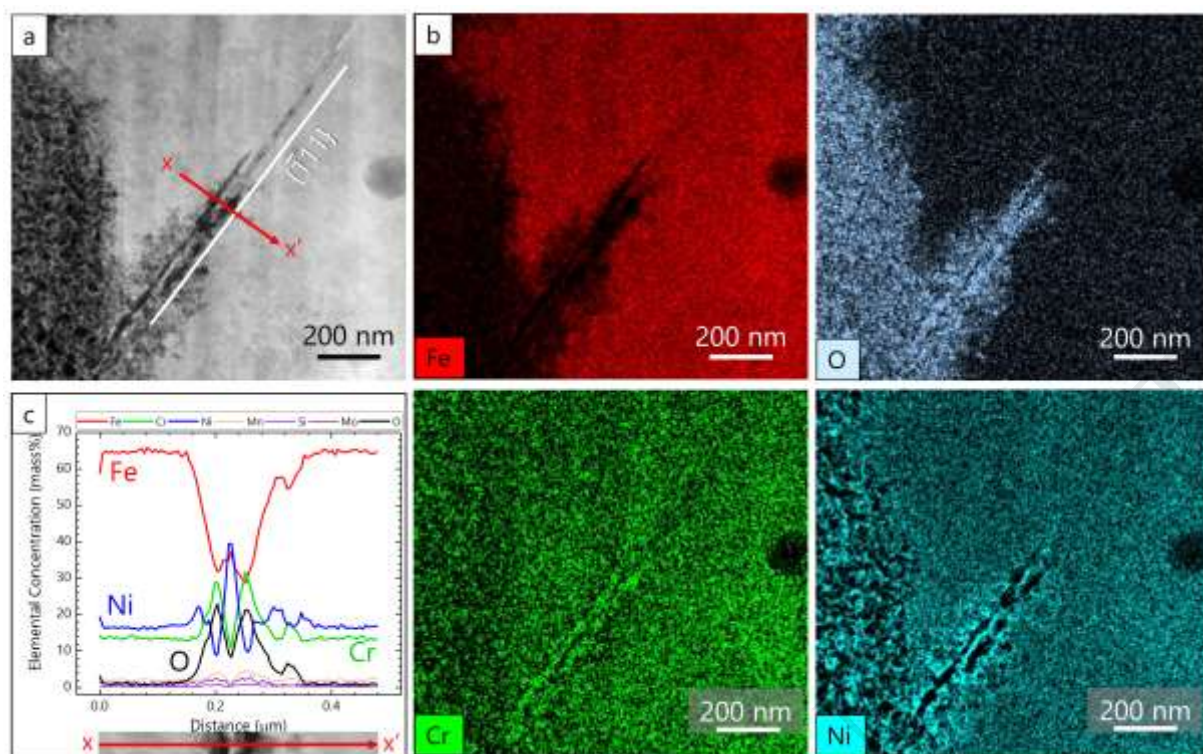
Fig. 10. (a) High-resolution STEM HAADF image showing the growth of an IOZ "needle" along a {$\bar{1}11$} steel plane, (b) STEM/EDS elemental maps of the area, and (c) STEM/EDS line scan across the "needle".
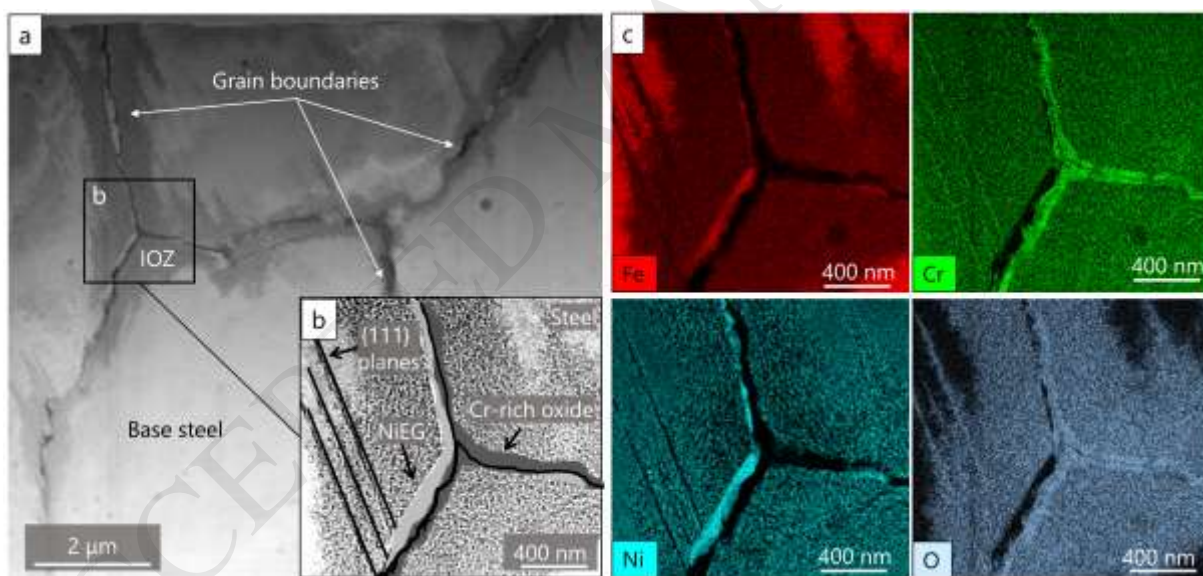
Fig. 11. (a) High-resolution STEM HAADF image showing the IOZ growing along grain boundaries, (b) idealised drawing and (c) STEM/EDS elemental maps (Fe/Cr/Ni/O) of area (b).
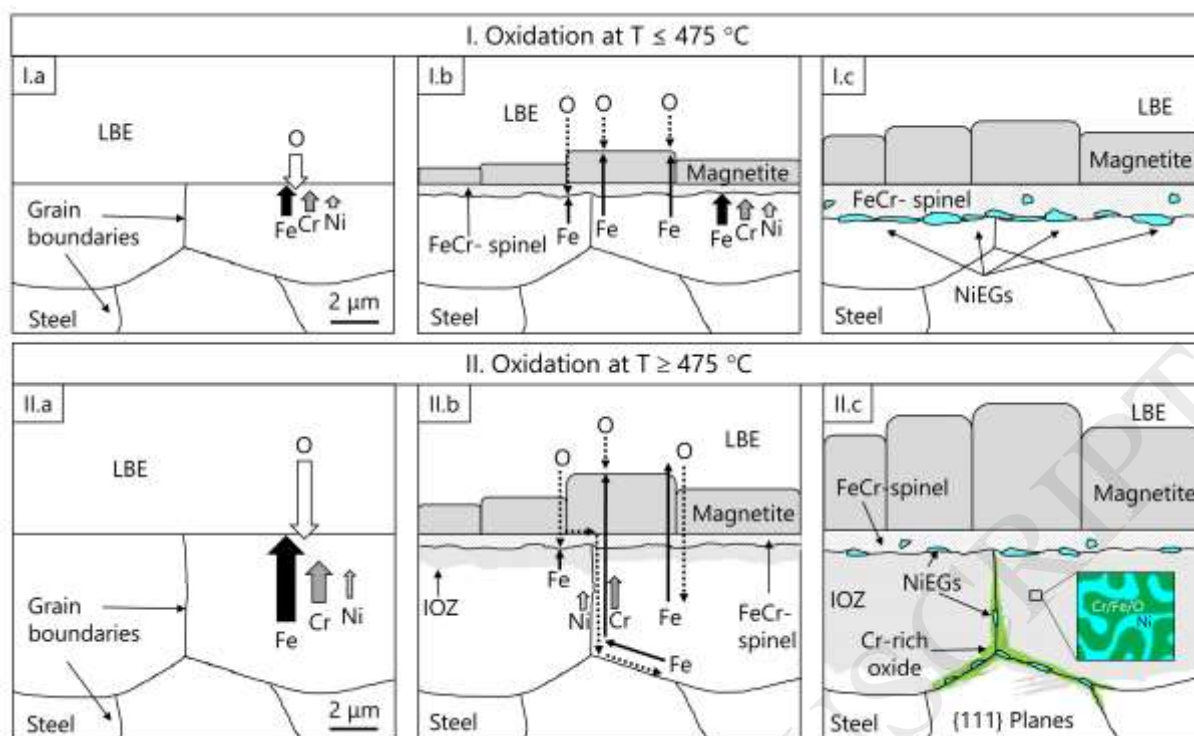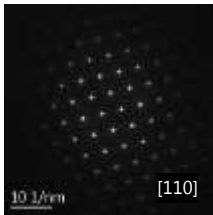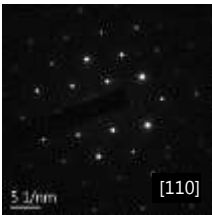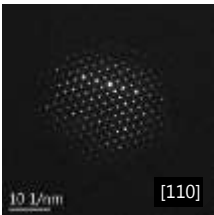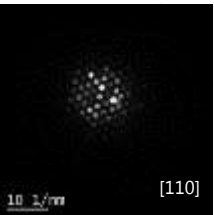
Fig. 12. I. Oxidation at $T \leq 475$ °C: (I.a) the onset of the oxidation process involves the inwards diffusion of O, which reacts with Fe and Cr at the LBE/steel interface; (I.b) growth of outer magnetite and inner FeCr-spinel scales; (I.c) formation of Ni-enriched grains (NiEGs) at the steel/Fe-Cr spinel interface. II. Oxidation at $T \geq 475$ °C: (II.a) similar onset of the oxidation process, faster diffusion of all elements; (II.b) growth of outer magnetite, inner FeCr-spinel, and IOZ; (II.c) IOZ growth along steel grain boundaries and {111} close-packed planes; steel grain boundary decoration by a Cr-rich oxide and NiEGs.

Table 1
SAED patterns, crystallography and chemical composition of the phases found in the DIN 1.4970 tube exposed at 450 °C.

	Base Steel	Ni-enriched grain (NiEG)	Magnetite (Fe_3O_4)	Fe-Cr spinel ($Fe_xCr_{3-x}O_4$)
Space group	*Fm-3m*	*Fm-3m*	*Fd-3m*	*Fd-3m*
SAED / Micro-diffraction	[110]	[110]	[110]	[110]
Concentration of main steel alloying elements (Fe/Cr/Ni) & O for the oxides (all in mass%)	Fe ≈ 65±2 Cr ≈ 15±0.5 Ni ≈ 15±0.5	Fe ≈ 32±2 Cr ≈ 5±1 Ni ≈ 60±5	Fe ≈ 68±5 Cr ≈ 4±1 Ni ≈ 1±0.5 O ≈ 27±2	Fe ≈ 25±3 Cr ≈ 45±5 Ni ≈ 1±0.5 O ≈ 29±2
Lattice parameter (nm)	0.359	0.365	0.859	0.880